designs

MDPI

Article

CAD-Based Design Optimization of Four-Bar Mechanisms: An Emergency Ventilator Case Study

Abdelmajid Ben Yahya [1,2], Nick Van Oosterwyck [1,2], Ferre Knaepkens [3], Simon Houwen [4,5], Stijn Herregodts [6], Jan Herregodts [6], Bart Vanwalleghem [4,5], Annie Cuyt [3,7] and Stijn Derammelaere [1,2,*]

1 Department of Electromechanics, Cosys-Lab, University of Antwerp, 2020 Antwerp, Belgium
2 AnSyMo/Cosys, Flanders Make, The Strategic Research Centre for the Manufacturing Industry, 3920 Lommel, Belgium
3 Department of Mathematics and Computer Science, University of Antwerp, 2020 Antwerp, Belgium
4 Department of Electrical Energy, Metals, Mechanical Constructions and Systems, Ghent University Campus Kortrijk, 8500 Kortrijk, Belgium
5 EEDT-MP, Flanders Make, The Strategic Research Centre for the Manufacturing Industry, 3920 Lommel, Belgium
6 Department of Human Structure and Repair, Ghent University, 9000 Gent, Belgium
7 College of Mathematics and Statistics, Shenzhen University, Shenzhen 518060, China
* Correspondence: stijn.derammelaere@uantwerpen.be

Abstract: The design optimization of mechanisms is promising as it results in more energy-efficient machines without compromising performance. However, machine builders do not apply state-of-the-art methods, as these algorithms require case-specific theoretical analysis. Moreover, the design synthesis approaches in the literature predominantly utilize heuristic optimizers, leading to suboptimal local minima. This paper introduces a widely applicable workflow, guaranteeing the global optimum. The constraints describing the feasible region of the possible designs are essential to find the global optimum. Therefore, kinematic analysis of the point-to-point planar four-bar mechanism is discussed. Within the feasible design space, objective value samples were generated through the CAD multi-body software. These motion simulations determine the required torque to fulfill the movement for a combination of design parameters. This replaces the cumbersome analytic derivation of the torque. This paper introduces sparse interpolation techniques to avoid brute force sampling of the design space. The advantage of this approach is that it is easily scalable to more design parameters, as the interpolation method minimizes the number of necessary samples. This paper explains the mathematical background of our developed interpolation approach. However, a step-by-step procedure is introduced to allow the employment of the interpolation technique by machine designers without the necessity to understand the underlying mathematics. Finally, the mathematical expression, obtained from the interpolation, enables applying global optimizers. In a case study of an emergency ventilator mechanism with three design parameters, 1870 CAD motion simulations allowed reducing the RMS torque of the mechanism by 67%.

Keywords: dimensional synthesis; four-bar linkage; optimization; mechanical systems; motion control

MSC: 70

Citation: Ben Yahya, A.; Van Oosterwyck, N.; Knaepkens, F.; Houwen, S.; Herregodts, S.; Herregodts, J.; Vanwalleghem, B.; Cuyt, A.; Derammelaere, S. CAD-Based Design Optimization of Four-Bar Mechanisms: An Emergency Ventilator Case Study. *Designs* **2023**, *7*, 38. https://doi.org/10.3390/designs7020038

Academic Editor: Bhanu Shrestha

Received: 30 January 2023
Revised: 21 February 2023
Accepted: 22 February 2023
Published: 3 March 2023

1. Introduction

The energy consumption of industrial machinery is a topic of primary importance due to environmental and economic considerations [1]. The 45% share of electric motors in the global electric consumption [2] supports the statement that any energy-saving method should be investigated thoroughly. The methodology proposed within this paper applies to all planar four-bar mechanisms with an imposed movement of the end-effector and/or output link BC (see Figure 1). The potential of this scope was indicated in [3–5],

stating that four-bar linkages are extensively used in practical engineering applications. Moreover, reciprocating Point-To-Point (PTP) machinery is progressively common within the industry [5].

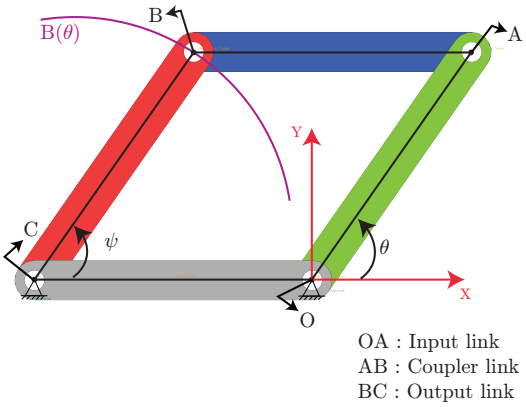

Figure 1. The considered design parameters (DPs) $|OA|$, $|AB|$, and $|BC|$ of a four-bar mechanism, in the present paper.

A required PTP displacement of the output link BC can be obtained with different link lengths. Therefore, the geometry parameters depicted in Figure 1 can be considered as design parameters (DPs) in a mechanism's optimization. The design optimization of a PTP mechanism can reduce the energy consumption (linked to the RMS motor torque) of electric machinery, as indicated in Figure 2. Awareness about the influence of machine components' geometry on energy consumption has recently attracted attention [6–8]. Mechanism models [9,10] replace prototyping, allowing the computational evaluation of multiple designs with limited costs.

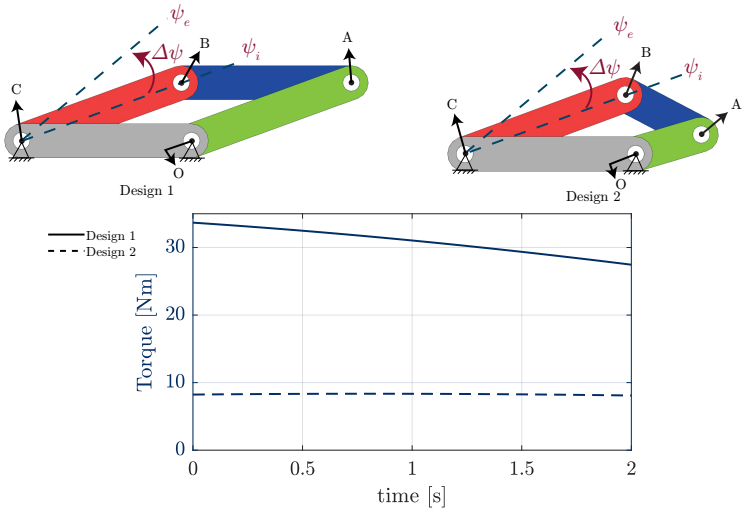

Figure 2. Defining certain lengths for the links of a four-bar mechanism influences the required torque to move the output link BC from ψ_i to ψ_e driven from Point O/Input Link OA.

An emergency ventilator was used as a validation case within this study. This mechanism was constructed during the first wave of the COVID-19 pandemic by a non-profit organization [11]. Having continuous (24/7) access to electricity is not obvious within low- and middle-income countries. Thus, having a mechanism that consumes a minimum of electric energy enabling the usage of batteries is highly relevant. Therefore, the objective of this study was to find the optimal design (lengths $|OA|$, $|AB|$ and $|BC|$) leading to a minimal T_{RMS} for a reciprocal four-bar mechanism.

State-of-the-art techniques generally use heuristic optimizers that cannot guarantee finding the global optimum [12]. However, the method introduced in this paper guarantees the global optimum in a build's convex hull by combining CAD motion simulations with sparse interpolation techniques. Once the constraints that limit the design space were defined, CAD motion simulations were used to sample the objective function. As such software is well known in the machine designer community, this approach allows broad industrial applicability by avoiding the cumbersome analytic derivation of the mechanism's dynamics. Furthermore, sparse interpolation avoids the infeasible computational burden of numerous CAD simulations. This interpolation method developed by the authors and introduced in this paper is described in depth. Moreover, a step-by-step procedure is presented to allow its application to any mechanism without the necessary in-depth insights into the underlying mathematics. Advances in sparse interpolation [13] make this approach very scalable to higher-dimensional optimizations. The interpolation model delivers a mathematical description that enables global optimizers such as INTLAB [14] even in high-dimensional problems. CAD motion simulations avoid cumbersome modeling, making this method also scalable to more complex mechanisms. In conclusion, one can state that the scalability of the proposed approach is enabled by the novel interpolation technique, which limits the number of CAD motion simulations to an absolute minimum.

In the literature [15], minimizing the driving torque of simplified mechanisms is accomplished by utilizing dynamic equations to predict the system dynamics. However, as noted by [5], the analytical computation of mechanism dynamics can become complex when dealing with systems containing a large number of components, as is commonly the case in industrial machinery. Alternative approaches, such as the use of generic equations of motion, have been proposed in the literature [16]. However, these methods still typically require information such as the reduced motor inertia as a function of motor position, which can be obtained by the method of kinetic energy [17], being cumbersome and error-prone. More specifically, studies [18,19] on generic dynamic equations for four-bar mechanisms still necessitate the determination of the center of gravity position and mass for each component of the mechanism with every design modification. This presents a challenge for machine builders, as it requires extensive case-specific analysis and data collection. Therefore, in engineering practice, it is standard to use Computer-Aided Design (CAD) software to build a dynamic model.

Moreover, References [18,20] did not define the feasible search domain nor include it in searching for the optimum result. The constraints that define the feasible design space are important as defects, giving infeasible designs [21], frequently occur in the kinematic mechanism synthesis of a four-bar linkage. The optimization algorithms of [15,18,22] ensure that the objective function converges towards a minimum, yet it is generally not guaranteed that the designed linkage will be feasible. Therefore, the necessary constraints should be added so that the optimal solution can fulfill the movement without inconveniences. A constrained global optimization algorithm requires a deterministic mathematical description of the constraints to find the global optimum. To the authors' knowledge, this has not been done yet in the literature [23].

Developing a four-bar mechanism that follows the desired output trajectory is a classic design problem that researchers have extensively explored [24–28]. However, all the methods above are not implementable in global optimizers as the algebraic expression (when provided) is only evaluated in discrete defined points $\begin{bmatrix} x_B(\theta) \\ y_B(\theta) \end{bmatrix}^*_{i\in\mathbb{N}}$ on the coupler curve $\mathbf{B}(\theta)$ (shown in Figure 1). Thus, these cannot deliver a deterministic mathematical description of the feasible design space, which is required.

This paper shows how CAD-based motion simulations combined with a novel sparse interpolation technique enable a global optimizer that guarantees the global optimum strictly within the convex hull covering the larger part of the feasible design space and thereby outperforming heuristic optimizers regarding energy savings.

The mechanical design of systems is mainly performed in CAD software. These CAD models include all required information (i.e., volume, mass, friction, damping, joints, etc.) to model the dynamics of a mechanism. This information is necessary to calculate the necessary torque of the mechanism through motion simulations. The required motor torque to move the mechanism is compulsory to evaluate a certain design with all attendant external forces on the mechanism. By driving the mechanism with the motion profile $\theta(t)$ at Point O (Figure 1), the location where the mechanism is driven in reality by a motor, the user can extract the necessary torque from the software (as in Figure 2) to fulfill the prescribed movement $\Delta\psi$ of the output link BC. Furthermore, within these motion simulations, the design parameters $|OA|$, $|AB|$, and $|BC|$ of the four-bar mechanism can be parameterized to simulate different designs. The objective value to be minimized by the optimizer is the RMS torque (T_{RMS}) value, necessary to drive the mechanism fulfilling an imposed PTP motion ($\Delta\psi$). The literature states that minimizing the T_{RMS} corresponds to reducing the energy losses in the system [5].

Hence, by calculating the RMS torque based on CAD simulations as elucidated in Section 2, the objective value for a certain design (i.e., certain values for the three design parameters $|OA|$, $|AB|$, and $|BC|$) is obtained. The whole simulation process to obtain the objective value for different design parameter combinations ($|OA|$, $|AB|$, and $|BC|$) is automated, as elucidated in [29]. Constraints on the design parameter values are necessary to define an area containing feasible designs, as discussed in Section 3, from which designs are selected to simulate their corresponding objective value (T_{RMS}). The proposed approach requires a kinematic analysis of the mechanism to find the constraints. However, this kinematic analysis is much more straightforward than modeling the necessary torque to drive the machine. Kinematic analysis is possible based on a graphical representation of the mechanism, as only the criteria described at the end of Section 3 have to be fulfilled. Modeling the necessary torque, however, requires defining position variable inertias, friction, possible non-linear external load forces, etc.; this is a severe hurdle for machine builders and an error-prone approach. All this is solved by relying on CAD motion simulations.

Computational simulation time becomes a burden as one design evaluation can take 1 min and 25 s on average. Therefore, a wise selection of the simulated designs within the feasible design space is essential. The brute force method requires an inconceivable number of g^d motion simulations, with g being the granularity of the sampling and d the number of design parameters. Even with state-of-the-art interpolation techniques [30], the construction of the objective function would require at least $(d+1).n^2.log^{2d-2}(n)$ samples, with n the total number of terms in the mathematical description of the objective function. In the case of the emergency ventilator, this would mean 782,933 samples are required. Therefore, the selection of samples is performed with certain rules in order to use an innovative multidimensional sparse interpolation approach [13]. This novel interpolation procedure, introduced in Section 4, allows obtaining a model of the objective function with a sparse sampling method within the feasible design space. This reduces the number of required samples to 618, with an additional 1252 validation samples. Limiting the number of samples (CAD motion simulations) to a bare minimum to model the objective function is a major enabler for a global optimizer. In this case, the number of necessary samples is reduced from 10,000,000 to 1870. While Section 4 discusses the interpolation technique and its underlying mathematics in depth, applying this technique only requires following the steps summarized at the end of Section 4.

2. CAD Motion Simulations

In kinematic analysis, the linkage dimensions $|OA|$, $|AB|$, $|BC|$, and $|OC|$ are known, and the resulting output motion $\psi(t)$ (and its derivatives) can be calculated. On the other hand, dimensional synthesis is regarded as the inverse, in which, for a specific output motion $\psi(t)$, the feasible dimensions of the linkages are obtained [31]. This paper is based on the dimensional synthesis of a planar four-bar function generation [32]. As shown in

Figure 3, the movement $\Delta\psi$ of the output linkage BC caused by $\theta(t)$ is described by a starting angle ψ_i and an end angle ψ_e. In this paper, the machine designer only defined an output motion $\psi(t)$, which results in a reciprocal movement between the positions ψ_i and ψ_e.

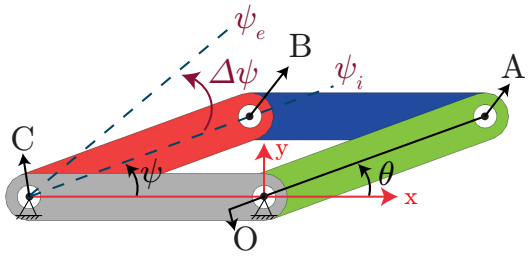

Figure 3. The output link BC requires a movement from ψ_i to ψ_e, which is performed by moving θ over a design-specific angle.

The validation case is clarified to make all the following more tangible. This mechanism, shown in Figure 4, can ventilate a patient by pressing the indenter into the bag, which causes airflow toward the patient. Figure 4 presents the CAD model of the emergency ventilator and illustrates that the red beam, connected to the indenter (i.e., the end-effector), moves by rotating Input Link OA around Point O. This is the point where an electric motor drives the mechanism. The red beam has two predefined angles: an angle δ_e that holds the mechanism in a position where the indenter touches the bag and an angle δ_i that corresponds to a position in which the air is compressed out of the bag. Figure 4 clearly shows that the mechanism is a four-bar linkage on which the method proposed in this paper can be applied.

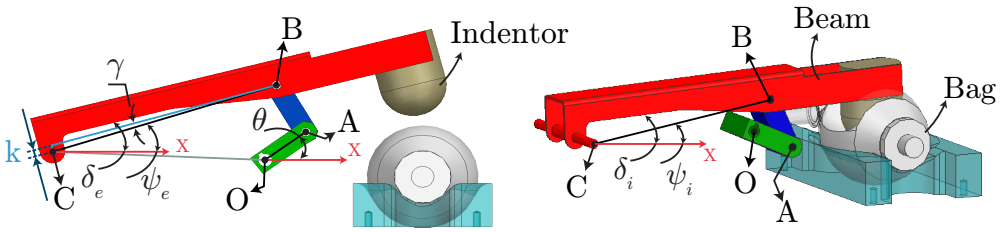

Figure 4. The used case within this research is an emergency ventilator developed by Gear Up Medical vzw [11]. One can see that the mechanism is from a four-bar type.

However, the output motion of the emergency ventilator is described by the angle δ (linked to the red beam), while the four-bar mechanism has an angle ψ that is linked to the output link BC. The relation between these angles is stated as

$$\psi = (\delta + \gamma) \tag{1}$$

where

$$\gamma = \sin\left(\frac{\mathrm{k}}{|\mathrm{BC}|}\right)$$

allows a conversion from δ to ψ. The parameters k and γ in Equation (1) (Figure 4) are constant values that change neither in the optimization, nor during the four-bar mechanism's movement.

A CAD motion simulation [33] can determine the necessary torque to drive the mechanism at Point O only if the required position profile $\theta(t)$ is known at that Point O. However, the user solely defines the required position profile of the end-effector, in this case $\delta(t)$. According to Equation (1), we obtain $\psi(t)$. The conversion of $\psi(t)$ to $\delta(t)$ depends on the values of the design parameters $|OA|$, $|AB|$, and $|BC|$. Therefore, each selected design was

analyzed by two motion simulations, as indicated in Figure 5. If the design is combined with the required output motion $\psi(t)$, the first kinematic motion simulation can extract the required motor position displacement $\theta(t)$. Subsequently, the motor motion profile $\theta(t)$ is used in the second motion simulation, determining the required driving torque. This process with kinematic simulation and subsequent torque calculation extracts the objective value for predefined designs, which is an approach that was explained in detail in [29].

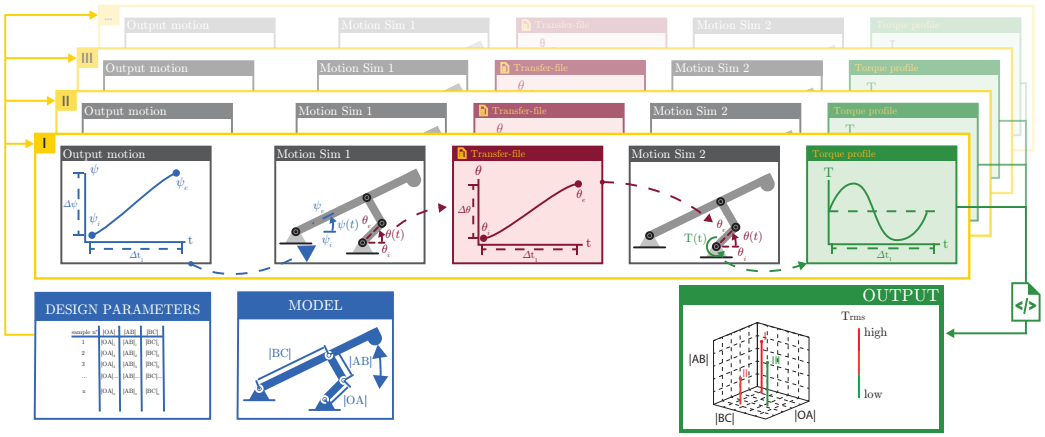

Figure 5. This approach performs the necessary driving torque calculation of the mechanism.

3. Design Parameter Constraints

3.1. Static Constraints of a Four-Bar Mechanism

The combinations of design parameters $|OA|$, $|AB|$, and $|BC|$, to consider in the workflow above, were chosen so that the designs were located within the feasible design space of the four-bar mechanism. Determine this region of feasible designs by looking for static constraints as a first step. The static constraint implies that only the designs that are assemblable for the maximal and minimal angle of the output link BC (ψ_i and ψ_e) can be part of the feasible design space. An example of a design that cannot be assembled in ψ_e due to the chosen values for DPs $|OA|$, $|AB|$, and $|BC|$ is illustrated in Figure 6. This shows that the input link OA' cannot be connected with to the coupler link A"B.

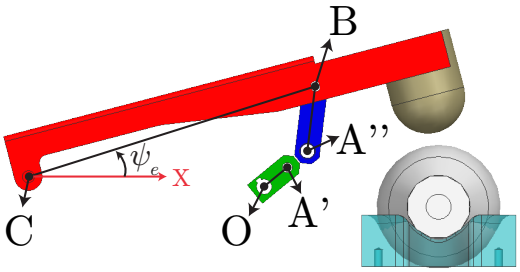

Figure 6. The combination of design parameters $|OA|$, $|AB|$, and $|BC|$ serves as an infeasible design that cannot be assembled in ψ_e.

This assemblability constraint defines the first boundaries on the design space illustrated in Figure 7 (left) (only in 2D for illustrative purposes). These boundaries were obtained through a position analysis of the four-bar mechanism for both beginning position ψ_i and ending position ψ_e. For the analysis of the ventilator, the origin of the fixed frame was placed in Joint O (the driver joint). Let θ be the angle of the input link OA measured relative to the x-axis and ψ the angle of the output link BC relative to the x-axis; see Figure 7 (right). The relation between the input angle θ and output angle ψ was obtained based on

the length of the coupler link $|AB|$, which stays fixed during the mechanism's movement [34]. Therefore, the analysis can start with

$$\left(\begin{bmatrix} x_B(\psi) \\ y_B(\psi) \end{bmatrix} - \begin{bmatrix} x_A(\theta) \\ y_A(\theta) \end{bmatrix}\right) \cdot \left(\begin{bmatrix} x_B(\psi) \\ y_B(\psi) \end{bmatrix} - \begin{bmatrix} x_A(\theta) \\ y_A(\theta) \end{bmatrix}\right) = |AB|^2 \tag{2}$$

where

$$\begin{array}{ll} x_A(\theta) = |OA| \cos(\theta) & x_B(\psi) = x_C + |BC| \cos(\psi) \\ y_A(\theta) = |OA| \sin(\theta) & y_B(\psi) = y_C + |BC| \sin(\psi). \end{array} \tag{3}$$

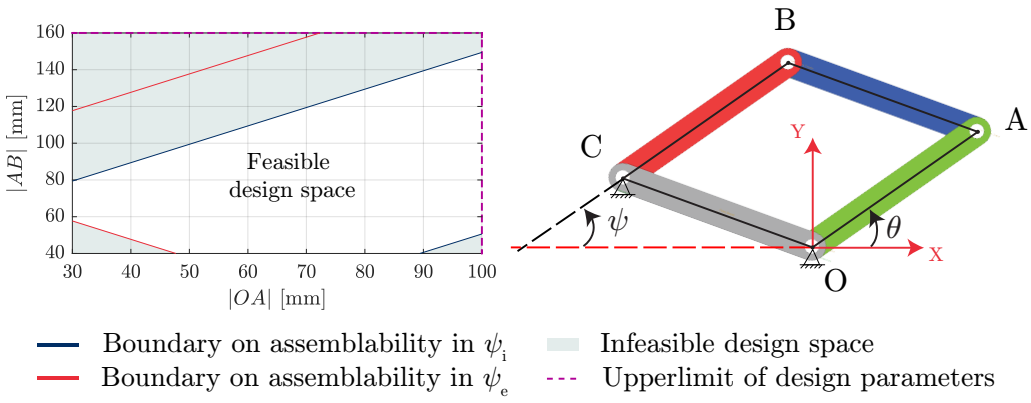

Figure 7. The static constraints (**left**), shown for 2 DPs, limit the design space to the area of the designs that reach the output link's (BC) starting and ending position (ψ_i and ψ_e).

By substitution of (3) in (2), the dependency of the input angle θ based on the output angle ψ is denoted as

$$\theta_{1,2}(\psi) = \text{atan2}(V(\psi), U(\psi)) \pm \arccos\left(\frac{W(\psi)}{\sqrt{U^2(\psi) + V^2(\psi)}}\right) + \pi \tag{4}$$

where

$$\begin{aligned} U(\psi) &= -2\, x_C\, |OA| - 2\, |OA|\, |BC| \cos(\psi) \\ V(\psi) &= -2\, y_C\, |OA| - 2\, |OA|\, |BC| \sin(\psi) \\ W(\psi) &= {x_C}^2 + {y_C}^2 + |OA|^2 + |BC|^2 - |AB|^2 + 2\cos(\psi)\, x_C\, |BC| \\ &\quad + 2\sin(\psi)\, y_C\, |BC|. \end{aligned} \tag{5}$$

Equation (4) allows the input angle θ derivation from the output angle ψ. The latter is the imposed output motion defined by the $\Delta\psi$ range. However, the mechanism can be assembled in two ways for a single output angle ψ, resulting in two possible solutions for (θ) in Equation (4). This is a consequence of having the possibility to construct the four-bar mechanism, with a specific angle ψ, with the output link BC on both sides of the diagonal OB, as shown in Figure 8. Both constructions, called the elbow-up OABC and elbow-down OA'BC, provide feasible solutions. The method proposed in the present paper applies to both configurations, yet it was chosen to focus on the elbow-up OABC, as it is the most-efficient one according to [35]. To obtain the corresponding θ_1, which is smaller than θ_2, the second term is subtracted from the first term in Equation (4).

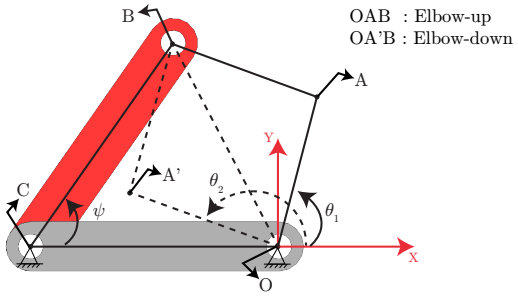

Figure 8. The elbow-up OAB and elbow-down OA'B are two possible constructions in which the four-bar linkage can be assembled for one ψ angle of the output link BC.

Regardless of the elbow configuration, the feasibility constraints due to the solvability of Equation (4) arise. A solution is found if the argument of arccos is in the range [−1,1]. Thus, a solution solely exists when the inequality constraint:

$$U^2(\psi) + V^2(\psi) - W^2(\psi) \geq 0 \tag{6}$$

is satisfied. In this way, an inequality constraint for the two output angles ψ that bring Point B farthest and closest to O must be established. Therefore, Equation (6) is evaluated for the maximal and minimal angle ψ_e and ψ_i. Thus, it considers the assemblability in the positions ψ_i and ψ_e.

$$U^2(\psi) + V^2(\psi) - W^2(\psi)\Big|_{\psi=\psi_i,\psi_e} \geq 0 \tag{7}$$

By fulfilling Equation (7), one can say that the designed mechanism is assemblable over its movement. This design lies within the area formed by the blue lines, which means that the mechanism is assemblable in ψ_i, and inside the area formed by red lines, as it is assemblable in ψ_e (see Figure 7).

3.2. Dynamic Constraints of a Four-Bar Mechanism

The aforementioned static constraints in Section 3.1 are not sufficient to exclude all infeasible designs. To ensure that the desired movement $\psi(t)$ of the output linkage BC is feasible, all defects during the movement should also be excluded. The three types of defects that can occur during the motion of a four-bar linkage are **branch**, **order**, and **circuit** defects. The broad review in [36] revealed that research about branch, order, and circuit defect avoidance is of great significance in the field of linkage syntheses. With a **branch** defect, the mechanism cannot perform the desired movement continuously. More specifically, four-bar linkages can move in two different ways. In Figure 9, the input link OA moves between its extreme positions (θ_{min} until θ_{max}), resulting in a change of the transmission angle ζ between 0 and π. The extreme input angle positions θ_{min} and θ_{max} correspond to an angle ζ equal to, respectively, π and 0. The movement is conducted by initiating the motion of the output link BC clockwise or counterclockwise around C. The movement in each initial direction around C (clockwise or counterclockwise) represents a separate branch. If the mechanism changes the branch while moving, a branch defect occurs for this linkage system design [37]. When a branch defect occurs, one can observe that the mechanism reaches the θ_{min} or θ_{max} position more than once during the movement. This branch defect results in a transmission angle ζ moving through 0 or π. Hence, when the mechanism moves through the positions ζ equal to 0 or π, a change in the direction of θ occurs.

Order defects appear if certain points $\begin{bmatrix} x_B(\theta) \\ y_B(\theta) \end{bmatrix}_{i\in\mathbb{N}}^{*}$ are not reached in a certain sequence or order [22]. Order defects were impossible in this study as a reciprocal mechanism was considered, which moves continuously (with a fixed motion profile $\pi(t)$) between the maximal and minimal angle ψ_e and ψ_i.

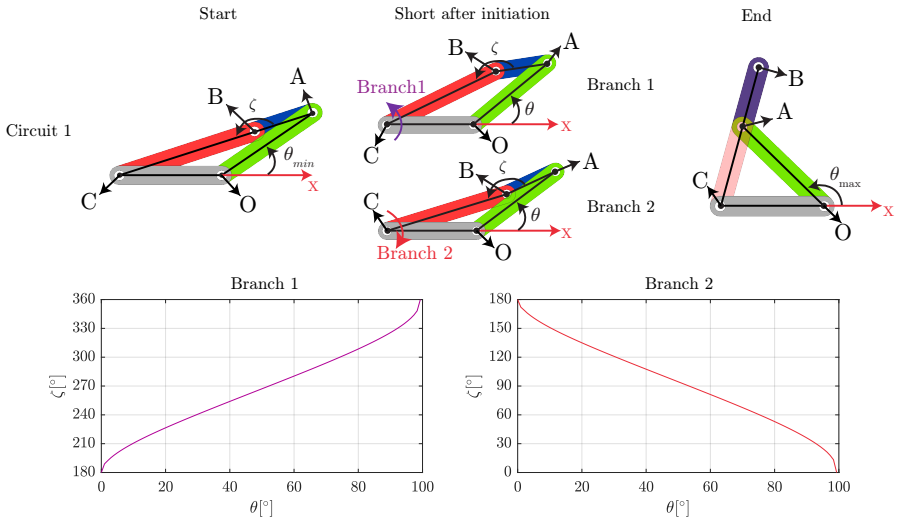

Figure 9. An example of a four-bar mechanism that has two connecting branches on the first circuit. It is shown that moving the mechanism from θ_{min} until θ_{max} corresponds to a movement of the transmission angle on Branch 1 from 180° to 360°, while on Branch 2, from 180° to 0°.

Figure 9 indicates that a **circuit** can exist out of two connected branches. Moreover, this design reveals that a mechanism can have another circuit in which the mechanism reaches whole other positions $\begin{bmatrix} x_B(\theta) \\ y_B(\theta) \end{bmatrix}^*_{i \in \mathbb{N}}$, as shown in Figure 10. The maximum number of circuits a four-bar mechanism can have is limited to two. The mechanism can move in each circuit separately without the necessity of disconnecting any joints [38]. A **circuit** defect arises when the linkage mechanism must be disassembled and placed in the other circuit, shown in Figure 11, to complete the motion. To obtain a circuit defect, θ should become bigger or smaller than θ_{max} (with $\zeta = 0$) or θ_{min} (with $\zeta = \pi$), respectively, to fulfill the desired movement of the output link BC ($\psi(t)$). A circuit defect has the same influence on θ as during a branch defect. In this paper, PTP movements with only a desired starting and ending point were considered. The movement takes place through the actuation of one joint, Point O. Therefore, the movement should stay within a single branch of a single circuit [39] (Figure 9 or 10).

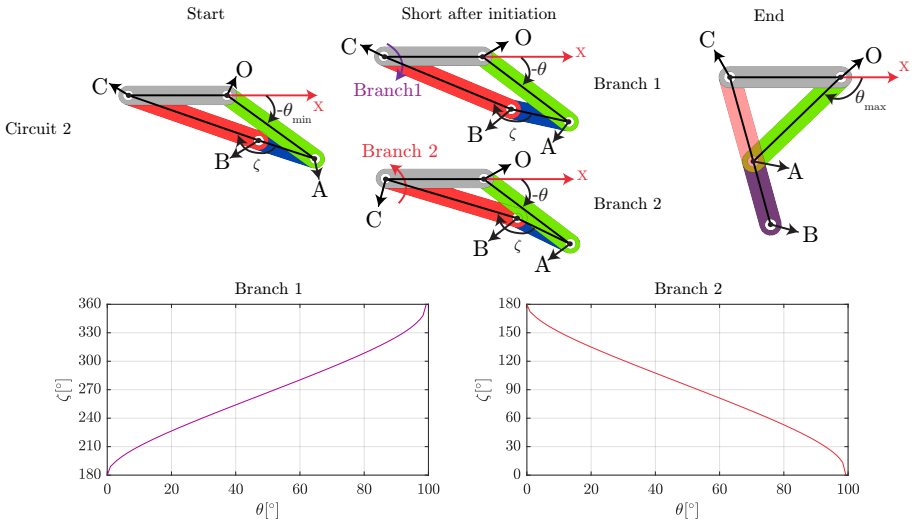

Figure 10. The second circuit of this specific four-bar design indicates that another circuit entails an entirely different range. Nonetheless, the circuit is also constructed by two connected branches with the same transition conditions for ζ.

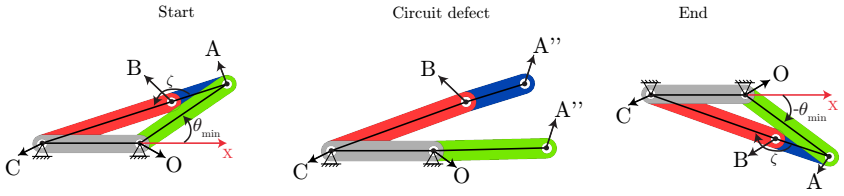

Figure 11. A designed linkage system that moves from one circuit to another must be disassembled, which is a circuit defect.

To eliminate the possible circuit and branch defects, dynamic constraints are created based on the consequence of a defect that changes the direction of the input angle θ. The calculations of the motor angle are always chosen for the elbow-up OABC. However, by altering the circuit, the configuration becomes an elbow-down in which θ moves in the other direction. Therefore, one can exclude branch and circuit defects by guaranteeing monotonicity in the motor position profile $\theta(t)$. The dynamic constraint:

$$sign\left(\dot{\theta}(\psi_i)\right) = sign\left(\dot{\theta}(\psi_e)\right) \tag{8}$$

will check if the first derivative of θ, in the starting and ending position ψ_i and ψ_e, alters its sign. Equation (8) is only applicable if the mechanism deals with an odd number of branch and or circuit defects while moving, as only then, a change of sign is detected. Nonetheless, the method is still applicable when an even number of defects occur, because a defect results in very high required driving torques for each sign change. The interpolation in Section 4 neglects these disproportional objective values. In that way, an even number of sign changes caused by an even number of defects will not affect the optimization. Therefore, all the constraints together indicate the feasible design spaces, as shown in Figure 12. Within the feasible design spaces, motion simulations are performed for certain samples to determine the objective value.

In summary, a mechanism design is feasible if it fulfills the following criteria:

- The design can be assembled at the location within its movement, where the output link BC is the closest to the driver joint O.
- The design can be assembled at the location within its movement, where the output link BC is farthest away from the driver joint O.
- The input angle $\theta(t)$ does not change direction while moving the output link BC from the starting to the ending point.

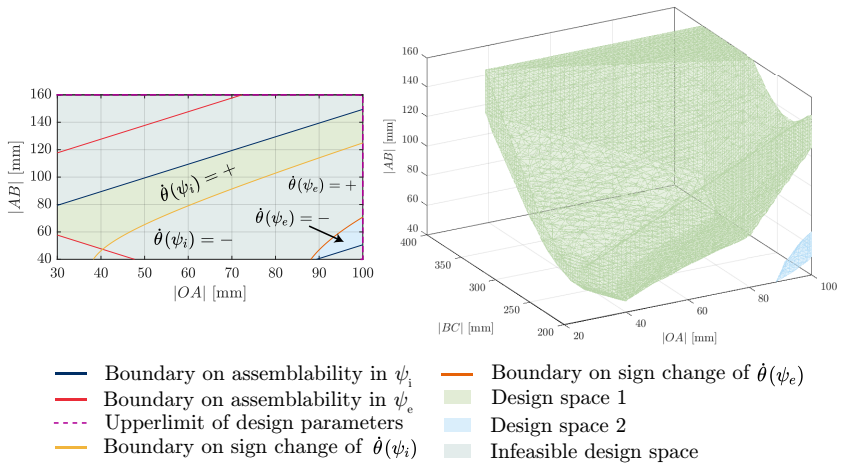

Figure 12. All constraints are shown for 2 DPs (**left**) and 3 DPs (**right**). The objects on the right are the feasible design spaces where the designs can perform the imposed reciprocal movement.

4. Multidimensional Sparse Interpolation

Determining the objective values using CAD multi-body simulations, for the three-dimensional design problem, in a brute force way would lead to a tremendous computational burden requiring 10,000,000 samples. Therefore, we relied on a sparse data fitting method to determine a mathematical model for the objective function $T_{RMS}(|OA|, |AB|, |BC|)$. This novel interpolation technique is now explained in detail, yet be aware that conveniently applying the method can be performed using the steps summarized at the end of this section. While several interpolation methods are characterized by a trade-off between model accuracy and computing cost, sparse interpolation does not involve such a compromise. The technique introduced here uses a divide-and-conquer approach [13,40] by splitting up the involved numerical linear algebra problems into smaller and better-conditioned independent sub-problems.

For this method, the objective value, within the feasible design space as defined in (7) and (8), is determined on l distinct lines in 3D space that are all parallel with a chosen vector $\Delta = (\Delta_u, \Delta_v, \Delta_w)$. We let $\delta^{(i)}, i = 0, \ldots, l-1$ indicate the 3D vector that the i-th parallel line is shifted over with respect to the line through the origin spanned by Δ for which we take $\delta^{(0)} = 0$. Then, the equidistant samples on these parallel lines, as depicted in Figure 13 (left), are denoted by:

$$T_k^{(i)} := T_{RMS}(k\Delta + \delta^{(i)}), \qquad i = 0, \ldots, l-1, \qquad k = 0, \ldots, N_i - 1.$$

As indicated further below, a translation of the domain to include the origin has no effect on the procedure, as this effect is at each step absorbed in the coefficients. Let us compactly denote the tuple of design variables $(|OA|, |BC|, |AB|)$ by

$$U = (u, v, w) := (|OA|, |BC|, |AB|)$$

and let $\langle \cdot, \cdot \rangle$ denote the standard inner product in 3D space. On each i-th parallel line, the samples $T_k^{(i)}$ can be modeled by the sparse interpolant:

$$T_{RMS,i}(U) = \sum_{j=1}^{n_i} \beta_j^{(i)} \exp\left(\langle \phi_j^{(i)}, U \rangle\right) \tag{9}$$

satisfying

$$T_k^{(i)} = \sum_{j=1}^{n_i} \beta_j^{(i)} \exp\left(k \langle \phi_j^{(i)}, \Delta \rangle\right), \qquad i = 0, \ldots, l-1, \qquad k = 0, \ldots, N_i - 1.$$

Note that the effect or influence of $\delta^{(i)}$ is absorbed into the coefficients $\beta_j^{(i)}$ in $T_{RMS,i}(U)$, which models the behavior of T_{RMS} on the i-th line.

The model for $T_{RMS,i}(U)$ can be computed using any of the existing 1D exponential fitting methods, such as [40–43]. The number of terms n_i in the sparse model can differ on each i-th line. The l individual models are only valid on their respective line spanned by Δ and shifted over $\delta^{(i)}$. Now, we need to blend these individual sparse models into an overall sparse model, valid in the convex hull of the l lines (blue area in Figure 13, right), which should cover the larger part of the region of interest. This requisite actually dictates the more proper choices for Δ and $\delta^{(i)}, i = 1, \ldots, l-1$.

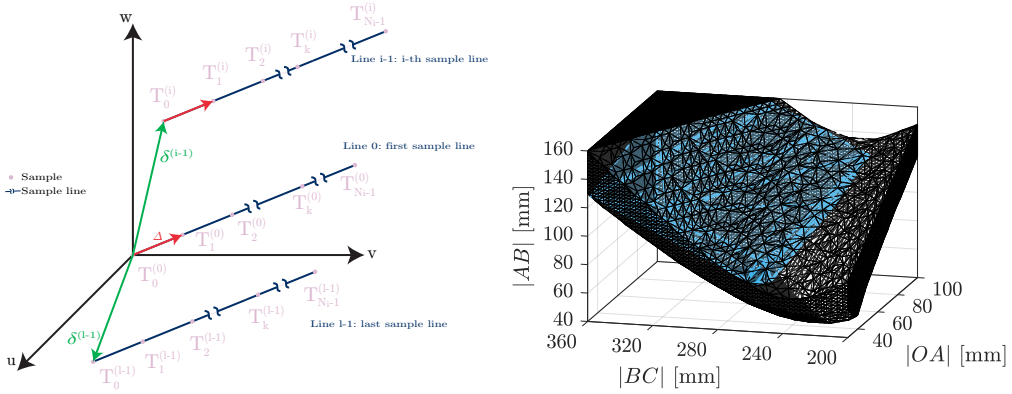

Figure 13. (**left**) All the samples located at points $k\Delta + \delta^{(i)}$. The convex hull, in blue, of the l lines covering the larger part of the design space (**right**).

In what follows, we considered every design parameter combination U in 3D space to lie on some line parallel with the one spanned by Δ, also if U is not an interpolation point. All the points on such a line take the form:

$$U + r\Delta, \qquad r \in \mathbb{R}. \tag{10}$$

The normal plane through the origin and orthogonal to Δ is given by the equation:

$$\Delta_u u + \Delta_v v + \Delta_w w = 0,$$

or more compactly:

$$\langle \Delta, U \rangle = 0.$$

The intersection point R of the normal plane with (10) is thus given by

$$\langle \Delta, R \rangle = 0, \qquad R = U + r\Delta,$$

or more explicitly:

$$R = U - \frac{\langle \Delta, U \rangle}{||\Delta||^2}\Delta. \tag{11}$$

Hence, the distance of U to this intersection point R, expressed as a multiple of $||\Delta||$, equals

$$d(u, v, w) = \frac{\langle \Delta, U \rangle}{||\Delta||^2}, \qquad U = (u, v, w)$$

and the points on the line given by (10) can be re-expressed as

$$R + d(U)\Delta \tag{12}$$

On each line through a point U parallel with Δ, the intersection point R with the normal plane, shown in Figure 14, is where $d(R) = 0$ on the line.

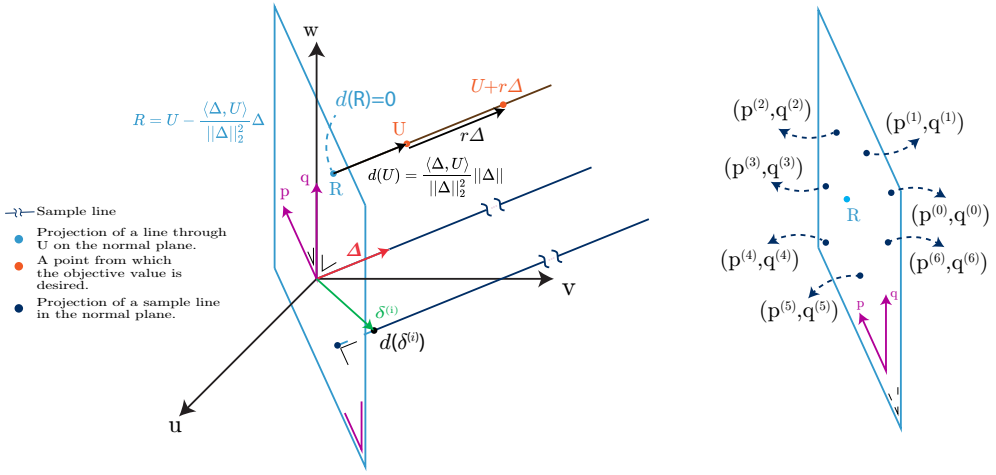

Figure 14. The intersection point R of the line $U + r\Delta$, parallel with Δ and through U, at the left. All $l = 7$ lines' intersection points $(p^{(i)}, q^{(i)})$ with the normal plane at the right.

Therefore, we propose a blended 3D model of the following form to represent the overall objective value T_{RMS}:

$$T_{RMS}(u,v,w) \approx \sum_{i=0}^{l-1} \sum_{j=1}^{n_i} b_j^{(i)}(u,v,w) \exp\Big(d(u,v,w)\langle \phi_j^{(i)}, \Delta\rangle\Big), \tag{13}$$

where the parameters $\phi_j^{(i)}$ and the value of $d(u,v,w)$ are already determined and where, furthermore, the overall model continues to interpolate the values $T_k^{(i)}$ in the sample points $k\Delta + \delta^{(i)}$. The blended model (13) coincides with the 1D models (9) on each parallel line, and in between the lines, the exponential terms fade in and out. Since

$$d(k\Delta + \delta^{(i)}) = k + d(\delta^{(i)})$$

this means

$$T_{RMS}(k\Delta + \delta^{(i)}) = \sum_{j=1}^{n_i} b_j^{(i)}(k\Delta + \delta^{(i)}) \exp\Big(d(\delta^{(i)})\langle \phi_j^{(i)}, \Delta\rangle\Big) \exp\Big(k\langle \phi_j^{(i)}, \Delta\rangle\Big). \tag{14}$$

In other words, on each data line, the model consists of only n_i terms, while in the convex hull of the parallel lines, it consists of $n_0 + \ldots n_{l-1}$ terms. Remember that all of l and $n_0, \ldots, n_{l-1}$ are small integer numbers.

From Equations (9) and (14), we consequently find

$$b_j^{(i)}(k\Delta + \delta^{(i)}) = \beta_j^{(i)} \exp\Big(-d(\delta^{(i)})\langle \phi_j^{(i)}, \Delta\rangle\Big),$$
$$k = 0, \ldots, N_i - 1, \quad i = 0, \ldots, \ell - 1, \quad j = 1, \ldots, n_i. \tag{15}$$

Note that $b_j^{(i)}(U)$ remains constant along each line of the form $R + d(U)\Delta$ and only varies with the projection R of that line onto the normal plane.

It remains to determine $b_j^{(i)}(u,v,w)$. These functions are determined by the interpolation conditions given in Equation (15). A simple model for $b_j^{(i)}(u,v,w)$ is a 2D polynomial interpolant $a_j^{(i)}(p,q)$, as we outline now. Let us denote the intersection point coordinates given in Equation (11) by $R = (r,s,t)$. The collection of points on a particular line perpendicular to the normal plane, say, here, through R, is entirely identified by the remaining two degrees of freedom that pinpoint the intersection point of such a line with the normal

plane. Since every point $U = (u, v, w)$ on the line perpendicular to the normal plane and passing through R satisfies the conditions:

$$\frac{u-r}{\Delta_u} = \frac{v-s}{\Delta_v} = \frac{w-t}{\Delta_w},$$

we can take any two of the values:

$$\begin{aligned} \Delta_v u - \Delta_u v &= r\Delta_v - s\Delta_u \\ \Delta_w u - \Delta_u w &= r\Delta_w - t\Delta_u \\ \Delta_w v - \Delta_v w &= s\Delta_w - t\Delta_v \end{aligned} \tag{16}$$

to characterize the full line. Over the whole of such a perpendicular line, the right-hand sides of Equation (16) are constant and independent of the points U on the line. The right-hand sides of Equation (16) are only determined by Δ and R. Say, for now, that we take the first two of (16), without any loss of generality: $p = \Delta_v u - \Delta_u v, q = \Delta_w u - \Delta_u w$. For the l parallel lines on which the samples were collected, we find

$$\left(p^{(i)}, q^{(i)}\right) = (\Delta_v \delta_u^{(i)} - \Delta_u \delta_v^{(i)}, \Delta_w \delta_u^{(i)} - \Delta_u \delta_w^{(i)}), \qquad i = 0, \ldots, l-1.$$

Let us abbreviate the values in the right-hand side of Equation (15) by $\alpha_j^{(i)}$ and replace $b_j^{(i)}(u, v, w)$ in Equation (13) by the more appropriate $a_j^{(i)}(p, q)$, since the interpolation conditions for $b_j^{(i)}(u, v, w)$ hold for a whole line and vary only with the intersection point of such a line with the normal plane:

$$T_{RMS}(u, v, w) \approx \sum_{i=0}^{l-1} \sum_{j=1}^{n_i} a_j^{(i)}(p, q) \exp\left(d(u, v, w)\langle \phi_j^{(i)}, \Delta \rangle\right). \tag{17}$$

Finally, the 2D polynomial interpolant:

$$a_j^{(i)}(p, q) = \sum_{h,\ell} \tau_{h\ell}^{(i,j)} T_h(p) T_\ell(q) \tag{18}$$

where $T_n(\cdot)$ denotes the well-known Chebyshev polynomial (of the first kind) of degree n, is computed from the interpolation conditions:

$$a_j^{(i)}\left(p^{(m)}, q^{(m)}\right) = \begin{cases} \alpha_j^{(i)}, & m = i \\ 0, & m \neq i, \end{cases} \qquad i, m = 0, \ldots, l-1, \qquad j = 0, \ldots, n_i. \tag{19}$$

We now apply the above to our four-bar problem. The region of interest for the design variables $|OA|, |AB|, |BC|$ and restricted by the conditions (7) and (8) is shown in Figure 15, and the sampling performed in this region is shown in red in Figure 15 (right). We took $l = 7$ and $\Delta = (0.000, 0.920, 0.503)$ to guarantee maximal coverage of the region of interest. Furthermore, the whole domain is translated over $-(31.000, 257.859, 72.705)$ to start sampling at the origin, in line with our description. Only 618 samples were determined by the simulations explained in Section 2, which shape the objective function. We found that $n_i = 5$ for all $i = 0, \ldots, 6$, thus yielding 7×5 terms in the global model $T_{RMS}(|OA|, |AB|, |BC|)$. The coefficients $a_j^{(i)}(p, q)$ were interpolated by a linear combination of the seven bivariate Chebyshev polynomials $T_m(p)T_n(q), 0 \leq m + n \leq 2$ and $T_2(p)T_1(q) + T_1(p)T_2(q)$. As a final step, we validated the blended model by collecting 1252 more simulation data on 10 other lines within the convex hull, along directions different from Δ. These evaluation directions are shown in purple in Figure 16 (left), and the result of this validation is shown in Figure 16 (right). In Figure 16 (right), the red and purple markers depict the simulated

data, and the blue markers represent the value computed from the blended model (17). Each partial curve shows the function values of $T_{RMS}(u, v, w)$ restricted to one of the lines where the samples were collected, either for interpolation (red) or validation (purple). The overall Root-Mean-Squared Error (RMSE) equals 0.0281Nm, indicating a very good fit. When restricting our attention to T_{RMS} values below 5—reasonable to locate a minimum—the RMSE reduces to 0.0153 Nm. Therefore, one can conclude that the global optimum within the convex hull can be found with an RMSE for the accuracy of 0.0153 Nm, being negligible.

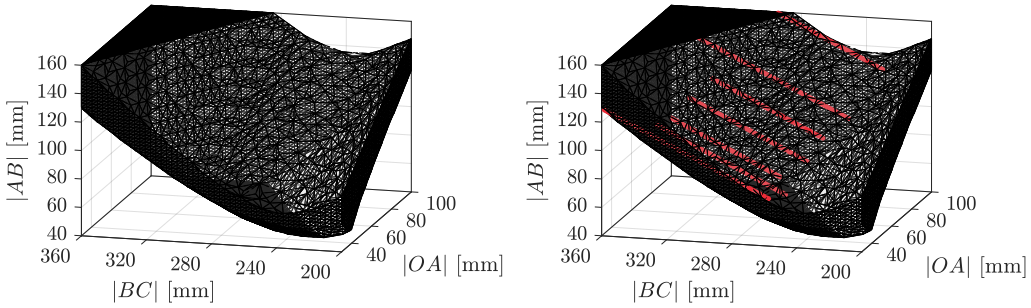

Figure 15. Region of interest delimited by (7) and (8) at the left and sampling locations on $l = 7$ parallel lines at the right in red.

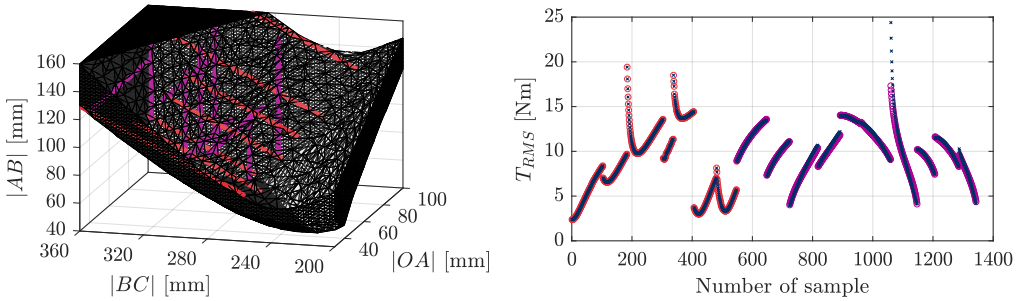

Figure 16. Validation directions at the left in purple and validation results of the blended model (17) at the right.

After this validation, we looked for a minimum of the modeled $T_{RMS}(u, v, w)$ (17) in the convex hull of the parallel lines shown in Figure 15 (right). This was fulfilled through a brute force evaluation of the objective function (17), in which 10,000,000 calculations were performed in 3 min. Thus, we can conclude that the most-time-consuming was the collection of all 1870 samples, in which generating a sample took 1 min and 25 s of simulation time on average. All aforementioned timings resulted from simulations conducted on a six-core Intel Core i7-9850H with 16GB RAM.

In summary, the interpolation model within this paper was obtained through the execution of Algorithm 1.

Algorithm 1: Constructing a blended sparse model for $T_{RMS}(u,v,w)$.

Data:

// Collect samples on l distinct parallel lines. Δ and $\delta^{(i)}$, $i=0,\ldots,l-1$, are chosen such that the convex hull covers the larger part of the region of interest.

$$T_k^{(i)} = T_{RMS}(k\Delta + \delta^{(i)}), \qquad k=0,\ldots,N_i-1, \quad i=0,\ldots,l-1.$$

Output:

// Sparse model

$$T_{RMS}(u,v,w) \approx \sum_{i=0}^{l-1}\sum_{j=1}^{n_i} a_j^{(i)}(p,q)\exp\Big(d(u,v,w)\langle\phi_j^{(i)},\Delta\rangle\Big).$$

Method:

// Define a function to measure the distance from the normal plane

$$d(u,v,w) \quad := \quad \frac{\langle\Delta,(u,v,w)\rangle}{\|\Delta\|^2}$$

Step 1

// Construct a 1D model for each line.

for $i=0,\ldots,l-1$ **do**

// Use any of the existing one-dimensional exponential fitting methods [40–43] on the data $T_k^{(i)}$, $k=0,\ldots,N_i-1$.

$$\Big(\beta_j^{(i)}\Big)_{j=1}^{n_i}, \Big(\exp(\langle\phi_j^{(i)},\Delta\rangle)\Big)_{j=1}^{n_i} \quad \longleftarrow \quad \texttt{ExponentialFit}\left(\left(T_k^{(i)}\right)_{k=0}^{N_i-1}, n_i\right)$$

end

Step 2

// Prepare to deal with the remaining 2 dimensions. Choose any 2 of the values of Equation (16). Here, the first 2 are chosen.

for $i=0,\ldots,l-1$ **do**

$$p^{(i)} \quad \longleftarrow \quad \Delta_v\delta_u^{(i)} - \Delta_u\delta_v^{(i)}$$

$$q^{(i)} \quad \longleftarrow \quad \Delta_w\delta_u^{(i)} - \Delta_u\delta_w^{(i)}$$

for $j=1,\ldots,n_i$ **do**

$$\alpha_j^{(i)} \quad \longleftarrow \quad \beta_j^{(i)}\exp\Big(-d(\delta^{(i)})\langle\phi_j^{(i)},\Delta\rangle\Big)$$

end

end

Step 3

// Blend 1D models by computing bivariate coefficient functions. Use the interpolation conditions in Equation (19) to retrieve the Chebyshev coefficients of Equation (18).

for $i=0,\ldots,l-1$ **do**

for $j=1,\ldots,n_i$ **do**

$$\left(\tau_{h\ell}^{(i,j)}\right)_{h,\ell} \quad \longleftarrow \quad \texttt{PolynomialFit}(\mathsf{InterpolationConditions}(i,j))$$

$$\alpha_j^{(i)}(p,q) \quad := \quad \sum_{h,\ell}\tau_{h\ell}^{(i,j)}T_h(p)T_\ell(q)$$

end

end

5. Conclusions

This paper proposed an industrially applicable and scalable approach that guarantees the global optimal design, strictly within the convex hull of the sampled lines, of a four-bar mechanism based on CAD motion simulations and sparse interpolation. The process of sampling the objective value T_{RMS} for a combination of design parameters $|OA|$, $|AB|$, and

$|BC|$ was automated by employing CAD multi-body motion simulations [29]. Through the utilization of the motion simulations, one does not perform the error-prone derivation of the cumbersome dynamic description of any mechanical system to obtain the motor torque. Subsequently, the constraints limiting the feasible design space were introduced based on the position analysis of the four-bar mechanism. These constraints guarantee that all designs the optimizer considers are assemblable and no circuit or branch defect will occur during the mechanism's movement.

The model reached a minimal value of 2.5989 Nm at $|OA| = 33.246$, $|BC| = 266.088$, and $|AB| = 79.435$. If the unconstrained design space were considered by a brute force approach, 10,000,000 objective value samples would be required to achieve the same result. As each objective value sample requires a simulation of approximately 1 min and 25 s, this would be practically impossible and seriously hamper the identification of the global optimum. However, thanks to the mathematical description of the design space constraints introduced in this paper, sparse interpolation can be applied. The innovative sparse interpolation technique described and applied here reduced the number of necessary simulations to only 618. The sparse interpolation method can be applied without an in-depth mathematical background, as it was developed as a step-by-step procedure requiring user input. This allowed us to identify the global optimal design within the obtained convex hull covering the larger part of the feasible design space. As shown in Table 1, the method clearly outperformed the best result (local optimum) obtained through the HEEDS Sherpa heuristic optimizer [44] and other attempts conducted in [29] to find a better result with broadly used optimizers. The obtained global optimum was 38% more efficient than the local optimum. Moreover, this result also reduced T_{max} by 67% compared to the original design, which means that the mechanism can operate with a smaller, and thus less-expensive, motor.

Table 1. Saving potential achieved with design optimization.

Design	$\|OA\|$ (mm)	$\|AB\|$ (mm)	$\|BC\|$ (mm)	T_{rms} (Nm)	T_{max} (Nm)	T_{rms} Savings (%)	T_{max} Savings (%)
Original	53	65	282	7.91	13.26	-	-
Local optimum	40.6	77.2	263.23	4.19	6.30	47	52.5
Global optimum	33.246	79.435	266.088	2.60	4.35	67	67

The results of this study confirmed the effectiveness of sparse interpolation in designing optimal mechanisms and suggested that this approach can be applied to more complex models in the future. To this end, we intend to extend our work beyond four-bar mechanisms, leveraging the scalability and flexibility of the CAD methodology and sparse interpolation, which have no inherent limitations in terms of model complexity. Our goal is to further optimize the optimization procedure by removing the need for prior knowledge of the constraint design space, which would eliminate the need for mechanism analysis.

Author Contributions: Conceptualization, A.B.Y., N.V.O., S.H. (Simon Houwen), B.V., S.D. and A.C.; methodology, A.B.Y., N.V.O., S.D., F.K. and A.C.; software, A.B.Y. and F.K.; formal analysis, A.B.Y.; investigation, A.B.Y.; material resources, J.H. and S.H. (Stijn Herregodts); data curation, A.B.Y.; writing—original draft preparation, A.B.Y. and A.C.; writing—review and editing, A.B.Y., N.V.O., S.D., and A.C.; visualization, A.B.Y.; supervision, S.D. and A.C. All authors have read and agreed to the published version of the manuscript.

Funding: Research funded by an internal PhD grant of the University of Antwerp [42418].

Data Availability Statement: The data presented in this study are available upon request from the corresponding author.

Conflicts of Interest: The authors declare that they have no conflict of interest.

References

1. Dornfeld, D. *Green Manufacturing: Fundamentals and Applications*; Springer: New York, NY, USA, 2013; Volume 9781441960, pp. 1–289. [CrossRef]
2. Waide, P.; Brunner, C.U. Energy-Efficiency Policy Opportunities for Electric Motor-Driven Systems. *Int. Energy Agency* **2011**, 132. [CrossRef]
3. Russell, K.; Sodhi, R.S. On the design of slider-crank mechanisms. Part I: Multi-phase motion generation. *Mech. Mach. Theory* **2005**, *40*, 285–299. [CrossRef]
4. Reis, V.L.; Daniel, G.B.; Cavalca, K.L. Dynamic analysis of a lubricated planar slider-crank mechanism considering friction and Hertz contact effects. *Mech. Mach. Theory* **2014**, *74*, 257–273. [CrossRef]
5. Berselli, G.; Balugani, F.; Pellicciari, M.; Gadaleta, M. Energy-optimal motions for Servo-Systems: A comparison of spline interpolants and performance indexes using a CAD-based approach. *Robot. Comput.-Integr. Manuf.* **2016**, *40*, 55–65. [CrossRef]
6. Carabin, G.; Wehrle, E.; Vidoni, R. A review on energy-saving optimization methods for robotic and automatic systems. *Robotics* **2017**, *6*, 39. [CrossRef]
7. Mashimo, T.; Urakubo, T.; Kanade, T. Singularity-based four-bar linkage mechanism for impulsive torque with high energy efficiency. *J. Mech. Robot.* **2015**, *7*, 1–8. [CrossRef]
8. Sheppard, P.; Rahimifard, S. Improving energy efficiency in manufacturing using peer benchmarking to influence machine design innovation. *Clean Technol. Environ. Policy* **2019**, *21*, 1213–1235. [CrossRef]
9. Oosterwyck, N.V.O.; Vanbecelaere, F.; Haemers, M.; Ceulemans, D.; Stockman, K.; Derammelaere, S. CAD Enabled Trajectory optimization and Accurate Motion Control for Repetitive Tasks. In Proceedings of the 2019 IEEE 15th International Conference on Control and Automation (ICCA), Edinburgh, UK, 16–19 July 2019; IEEE: Piscataway Township, NJ, USA, 2019; pp. 387–392. [CrossRef]
10. Oosterwyck, N.V.O.; Yahya, A.B.Y.; Cuyt, A.; Derammelaere, S. CAD based trajectory optimization of PTP motions using chebyshev polynomials. In Proceedings of the 2020 IEEE/ASME International Conference on Advanced Intelligent Mechatronics (AIM), Boston, MA, USA, 6–9 July 2020; pp. 403–408. [CrossRef]
11. Herregodts, J.; Herregodts, S. Gear up Medical. 2019. Available online: https://www.coronaventilator.be/ (accessed on 29 January 2023).
12. Piazzi, A.; Visioli, A. Global minimum-time trajectory planning of mechanical manipulators using interval analysis. *Int. J. Control* **2010**, *71*, 631–652. [CrossRef]
13. Cuyt, A.; Shin Lee, W. Multivariate exponential analysis from the minimal number of samples. *Adv. Comput. Math.* **2018**, *44*, 987–1002. [CrossRef]
14. Rump, S.M. INTLAB—INTerval LABoratory. *Dev. Reliab. Comput.* **1999**, 77–104. [CrossRef]
15. El-Kribi, B.; Houidi, A.; Affi, Z.; Romdhane, L. Application of multi-objective genetic algorithms to the mechatronic design of a four bar system with continuous and discrete variables. *Mech. Mach. Theory* **2013**, *61*, 68–83. [CrossRef]
16. Oosterwyck, N.V.O.; Vanbecelaere, F.; Knaepkens, F.; Monte, M.; Stockman, K.; Cuyt, A.; Derammelaere, S. Energy optimal point-to-point motion profile optimization. *Mech. Based Des. Struct. Mach.* **2022**, *47*, 1–18. [CrossRef]
17. Vanbecelaere, F.; Derammelaere, S.; Nevaranta, N.; Viaene, J.D.; Verbelen, F.; Stockman, K.; Monte, M. Online Tracking of Varying Inertia using a SDFT Approach. *Mechatronics* **2020**, *68*, 102361. [CrossRef]
18. Affi, Z.; El-kribi, B.; Romdhane, L. Advanced mechatronic design using a multi-objective genetic algorithm optimization of a motor-driven four-bar system. *Mechatronics* **2007**, *17*, 489–500. [CrossRef]
19. Dopico, D.; Sandu, A.; Sandu, C. Adjoint sensitivity index-3 augmented Lagrangian formulation with projections. *Mech. Based Des. Struct. Mach.* **2022**, *50*, 48–78. [CrossRef]
20. Rayner, R.; Sahinkaya, M.N.; Hicks, B. Combining Inverse Dynamics with tRaditional Mechanism Synthesis to Improve the Performance of High Speed Machinery. In Proceedings of the ASME 2008 Dynamic Systems and Control Conference. ASME 2008 Dynamic Systems and Control Conference, Parts A and B, Ann Arbor, MI, USA, 20–22 October 2008; ASME: New York, NY, USA, 2009; pp. 599–606. [CrossRef]
21. Hernández, A.; Muñoyerro, A.; Urízar, M.; Amezua, E. Comprehensive approach for the dimensional synthesis of a four-bar linkage based on path assessment and reformulating the error function. *Mech. Mach. Theory* **2021**, *156*, 104126. [CrossRef]
22. Gogate, G.R.; Matekar, S.B. Optimum synthesis of motion generating four-bar mechanisms using alternate error functions. *Mech. Mach. Theory* **2012**, *54*, 41–61. [CrossRef]
23. Shen, Q.; Lee, W.T.; Russell, K. On adjustable planar four-bar motion generation with order, branch and circuit defect rectification. *J. Mech. Robot.* **2015**, *7*, 34501. [CrossRef]
24. Hrones, J.A.; Nelson, G.L. *Analysis of the Four-Bar Linkage: Its Application to the Synthesis of Mechanisms*; Technology Press of the Massachusetts Institute of Technology: Cambridge, MA, USA, 1978.

25. Jaiswal, A.; Jawale, H.P. Comparative study of four-bar hyperbolic function generation mechanism with four and five accuracy points. *Arch. Appl. Mech.* **2017**, *87*, 2037–2054. [CrossRef]
26. Bai, S.; Angeles, J. Coupler-curve synthesis of four-bar linkages via a novel formulation. *Mech. Mach. Theory* **2015**, *94*, 177–187. [CrossRef]
27. Li, X.; Wei, S.; Liao, Q.; Zhang, Y. A novel analytical method for four-bar path generation synthesis based on Fourier series. *Mech. Mach. Theory* **2020**, *144*, 103671. [CrossRef]
28. Li, X.; Wei, S.; Liao, Q.; Zhang, Y. A novel analytical method for function generation synthesis of planar four-bar linkages. *Mech. Mach. Theory* **2016**, *101*, 222–235. [CrossRef]
29. Yahya, A.B.Y.; Oosterwyck, N.V.O.; Herregodts, J.; Herregodts, S.; Houwen, S.; Vanwalleghem, B.; Derammelaere, S. An Industrial Applicable Approach towards Design Optimization of a Mechanism: A Coronaventilator Case Study. *arXiv* **2022**, arXiv:2207.14537.
30. Sauer, T. Prony's method in several variables: Symbolic solutions by universal interpolation. *J. Symb. Comput.* **2018**, *84*, 95–112. [CrossRef]
31. Lee, W.T.; Russell, K. Developments in quantitative dimensional synthesis (1970-present): Four-bar motion generation. *Inverse Probl. Sci. Eng.* **2018**, *26*, 133–148. [CrossRef]
32. Lee, W.T.; Russell, K. Developments in quantitative dimensional synthesis (1970-present): Four-bar path and function generation. *Inverse Probl. Sci. Eng.* **2018**, *26*, 1280–1304. [CrossRef]
33. Simcenter 3D for Motion Simulation. 2020. Available online: www.cardsplmsolutions.com/nl/producten/simcenter-3d (accessed on 29 January 2023).
34. McCarthy, J.M.; Soh, G.S. *Geometric Design of Linkages*, 2nd ed.; Springer: New York, NY, USA, 2010; p. 477. [CrossRef]
35. Srivatsan, R.A.; Bandyopadhyay, S. On the position kinematic analysis of MaPaMan: A reconfigurable three-degrees-of-freedom spatial parallel manipulator. *Mech. Mach. Theory* **2013**, *62*, 150–165. [CrossRef]
36. Balli, S.S.; Chand, S. Defects in link mechanisms and solution rectification. *Mech. Mach. Theory* **2002**, *37*, 851–876. [CrossRef]
37. Singh, R.; Chaudhary, H.; Singh, A.K. Defect-free optimal synthesis of crank-rocker linkage using nature-inspired optimization algorithms. *Mech. Mach. Theory* **2017**, *116*, 105–122. [CrossRef]
38. Chase, T.R.; Mirth, J.A. Circuits and Branches of Single-Degree-of-Freedom Planar Linkages. *ASME J. Mech. Des.* **1993**, *115*, 223–230. [CrossRef]
39. Feki, M.S.; Chaari, F.; Abbes, M.S.; Viadero, F.; Rincon, A.F.D.; Haddar, M. Identification of a Usable Six-Bar Linkage for Dimensional Synthesis. *Mech. Mach. Sci.* **2013**, *7*, 311–318. [CrossRef]
40. Briani, M.; Cuyt, A.; Knaepkens, F.; shin Lee, W. VEXPA: Validated EXPonential Analysis through regular sub-sampling. *Signal Process.* **2020**, *177*, 107722. [CrossRef]
41. Roy, R.; Kailath, T. ESPRIT-estimation of signal parameters via rotational invariance techniques. *IEEE Trans. Acoust. Speech, Signal Process.* **1989**, *37*, 984–995. [CrossRef]
42. Schmidt, R. Multiple emitter location and signal parameter estimation. *IEEE Trans. Antennas Propag.* **1986**, *34*, 276–280. [CrossRef]
43. Steedly, W.M.; Ying, C.; Moses, R. Statistical analysis of TLS-based prony techniques. *Automatica* **1994**, *30*, 115–129. [CrossRef]
44. Technology, R.C. *SHERPA, an Efficient and Robust Optimization (Search) Algorithm*; Red Cedar Technology: Lansing, MI, USA, 2014; pp. 1–3.